Electronic Supplementary Information (ESI)

Anchoring highly dispersed metal nanoparticles by strong electrostatic adsorption (SEA) on dealuminated Beta zeolite for catalysis

Run Zou[1,2], Gabriell Bramley[3], Shanshan Xu[1], Sarayute Chansai[1], Monik Panchal[4], Huanhao Chen[5], Yangtao Zhou[2], Pan Gao[6], Guangjin Hou[6], Stuart M. Holmes[1], Christopher Hardacre[1], Yilai Jiao[2]*, Andrew Logsdail[3]*, Xiaolei Fan[1,7]*

[1]Department of Chemical Engineering, School of Engineering, The University of Manchester, Oxford Road, Manchester, M13 9PL, United Kingdom

[2]Shenyang National Laboratory for Materials Science, Institute of Metal Research Chinese Academy of Sciences, 72 Wenhua Road, Shenyang, 110016, China

[3]Cardiff Catalysis Institute, School of Chemistry, Cardiff University, Park Place, Cardiff, CF103AT, Wales, United Kingdom

[4]Department of Chemistry, Durham University, Stockton Road, DH1 3LE, United Kingdom

[5]State Key Laboratory of Materials-Oriented Chemical Engineering, College of Chemical Engineering, Nanjing Tech University, Nanjing 211816, China

[6]State Key Laboratory of Catalysis, National Laboratory for Clean Energy, 2011-Collaborative Innovation Center of Chemistry for Energy Materials, Dalian Institute of Chemical Physics, Chinese Academy of Sciences, Zhongshan Road 457, Dalian 116023, China

[7]Nottingham Ningbo China Beacons of Excellence Research and Innovation Institute, University of Nottingham Ningbo China, 211 Xingguang Road, Ningbo 315100, China

*Corresponding Authors' emails: yljiao@imr.ac.cn (Y.J.); LogsdailA@cardiff.ac.uk (A.L.); Xiaolei.fan@manchester.ac.uk (X.F.)

Content

Catalyst preparation

Chemicals

All chemicals were obtained from commercial suppliers and used as received. Zeolite NH_4-Beta (CP814E) was obtained from Zeolyst International. Nitric acid (HNO_3, 70 wt.%), ammonium hydroxide (NH_4OH, 25 wt.%), nickel chloride hexahydrate ($NiCl_2 \cdot 6H_2O$) and nickel nitrate hexahydrate ($Ni(NO_3)_2 \cdot 6H_2O$, 99 wt.%) were purchased from Sigma Aldrich. All the gases (including H_2, CO_2, CH_4 and CO) used for characterization and catalysis have the purity of 99.99%.

Dealuminated Beta zeolite

Dealumination of zeolite Beta (**deAl-Beta**) was achieved by treating 2 g of the H-Beta (obtained by calcination of ammonium-type Beta under 550 °C for 5 h) with 40 mL concentrated HNO_3 (13 mol/L) at 100 °C for 24 h under magnetic stirring (350 rpm)[1]. After the acid treatment, the resulting sample was washed with Milli-Q water and separated by centrifugation until the pH value of supernatant was around 7–8, and then dried at 90 °C in an oven overnight.

Zeolite-supported metal nanoparticles (NPs)

Zeolite-supported metal NPs were synthesized by either strong electrostatic adsorption (**SEA**) or impregnation (**IM**). In a typical SEA synthesis, the metal-ammine precursor solution was made by dissolving certain amount of metal precursor (e.g., 164 mg of $NiCl_2 \cdot 6H_2O$ or 198 mg of $Ni(NO_3)_2 \cdot 6H_2O$) in diluted ammonia solution (total volume of 250 mL containing 240 mL of deionised water and 10 mL of ammonium hydroxide, giving a pH of about 12) to give the theoretical metal loading of 10 wt.%. Then 0.4 g deAl-Beta support was added to above solution system with thoroughly stirring at 300 rpm (by a magnetic stirrer) for 20 min at room temperature to allow the adsorption of metal-ammine cations (i.e., $Ni(NH_3)_6^{2+}$) onto the electronegative zeolite support. The metal ion-containing zeolite powder was recovered by centrifugation (without washing) and dried at room temperature overnight. The solid was further placed in a drying oven at 120 °C for 4 h before being reduced in hydrogen flow (as described below). The final products after reduction were named **Ni-Cl@deAl-Beta-SEA and/or Ni-NO$_3$@deAl-Beta-SEA**.

The as-prepared Ni catalysts were pelletized (355–500 μm, about 0.2 g sample was pressed with applied pressure of 3000 kg) before reduced in a Carbolite tube furnace using pure H_2 (flow rate = 100 mL/min) at 500 °C for 1 h (at 5 °C/min).

Comparatively, conventional impregnation (**IM**) was also employed to prepare the control catalyst, that is, **Ni-Cl/deAl-Beta-IM and/or Ni-NO$_3$/deAl-Beta-IM**. In brief, 0.4 g of support (e.g., deAl-Beta and/or H-Beta) was dispersed in 30 mL water to form the zeolite suspension before the addition of the precursor solution (164 mg of $NiCl_2 \cdot 6H_2O$ or 198 mg of $Ni(NO_3)_2 \cdot 6H_2O$ in 2 mL water) dropwise to achieve the theoretical Ni loading of 10 wt.%. The mixture was mixed with magnetic stir (350 rpm) for 12 h at room temperature, and then placed in an oil bath (at 70 °C) to evaporate the water slowly (overnight). Lastly, the final product was obtained under the same thermal and reduction treatments used by the SEA protocol.

Preparation of supported Ni catalysts on deAl-Beta with less hydroxyl groups (after calcination of the pristine deAl-Beta at 550 °C for 6 h with ramping rate of 5 °C/min) using $Ni(NO_3)_2 \cdot 6H_2O$ as precursor was followed the same procedure stated above. The resulting catalyst is denoted as **Ni-**

NO$_3$@calcinated deAl-Beta-SEA.

Characterization of materials

Powder X-ray diffraction (XRD). Crystalline property of the materials was analysed by X-ray diffraction (XRD, Bruker, D8 advance) with a step size of 0.02° and scanning rate of 8°/min at room temperature using Cu Kα line (λ = 1.5418 Å).

Nitrogen (N$_2$) adsorption-desorption. Isotherms of the materials were measured using a surface area analyser (Micromeritics, ASAP 2920) at −196 °C. Prior to the N$_2$ physisorption, the sample was outgassed overnight at 300 °C under vacuum. The Brunauer-Emmett-Teller (BET), t-plot and Barrett-Joyner-Halenda (BJH) models were used to estimate specific surface area, pore volume, as well as pore size distribution.

Inductively coupled plasma optical emission spectrometer (ICP-OES). The silicon to alumina ratio (SAR) and actual Ni content of the zeolite/catalysts was determined by inductively coupled plasma optical emission spectrometer (Varian 710-es). Prior to analysis, catalyst (ca. 20 mg) was digested by microwave digestion (ETHOS UP microwave digester) in mixture of aqua regia and hydrofluoric acid (total volume of 12 mL, HCl: HNO$_3$: HF = 1: 3: 1).

Scanning electron microscope and energy dispersive X-ray spectroscopy (SEM-EDS). The morphology and surface elemental distribution of the materials were studied by SEM-EDS (FEI Quanta 250) at 20 kV. Before SEM-EDS analysis, the powder sample was adhered on a stub with double-coated carbon conductive tape before coating with Pt (about 8 nm) on a Pt sputter coater.

Transmission electron microscopy (TEM). The microscopic structural details of the materials were observed by high-angle annular dark-scanning transmission electron microscopy (HAADF-STEM, Fei Tecnai F20) at 200 kV. Before TEM analysis, the sample was dispersed in ethanol (which was sonicated for 5 min in an ultrasonic bath), and a droplet of the solution was casted on a carbon-coated mesh grid.

Hydrogen temperature-programmed reduction (H$_2$-TPR). H$_2$-TPR was measured by a chemisorption analyser (Micromeritics, AutoChem II 2920) equipped with a thermal conductivity detector (TCD). About 50 mg of the as-prepared Ni catalysts (after SEA and drying at 120 °C for 4 h) was used for each H$_2$-TPR analysis. The samples were pretreated at 300 °C in Ar (50 mL/min) for 1 h before analysis. The measurement was conducted in 10 vol.% Ar-balanced H$_2$ (50 mL/min) from 100 to 800 °C with ramping rate of 5 °C/min.

Hydrogen temperature-programmed reduction-mass spectrum (H$_2$-TPR-MS). H$_2$-TPR-MS was carried out on a fixed-bed flow reactor system with a quartz tube (inner diameter of 4 mm) at atmospheric pressure. About 50 mg of the as-prepared Ni catalysts (after SEA and drying at 120 °C for 4h) with 355–500 μm pellets were placed between plugs of quartz wool, and a K-type thermocouple was placed in the centre of the catalyst bed. TPR was performed in Ar-balanced H$_2$ (1 vol.%) with flow rate of 100 mL/min and temperature ramping rate of 10 °C /min (from 50 to 650 °C). The H$_2$, NH$_3$, H$_2$O, N$_2$ and HCl in the outlet stream (m/z of 2, 15, 18, 28 and 38) was analysed online using a mass spectrometer (Hiden Analytical HPR 20).

X-ray photoelectron spectrometer (XPS). XPS spectra of the reduced Ni catalysts were recorded on a Thermo Scientific EscaLab 250Xi apparatus with a focused monochromatic Al Kα X-ray (1486.6 eV) source for excitation. The binding energy of the chemical species was calibrated using the C 1s peak at 284.8 eV as an internal standard. The percentages of the individual elements were fitted by

analysing the areas of the respective peaks (CasaXPS). The Ni/Si surface ratio was calculated from the XPS survey using the 'Library' function by integrating the peak area of Ni 2p (B.E. = 852, R.S.F. = 4.044) and Si 2p (B.E. = 99, R.S.F. = 0.328).

Magic angle spinning nuclear magnetic resonance spectra (MAS NMR). ^{1}H MAS NMR were acquired on a spectrometer (Bruker 400 MHz) equipped with a wide-bore 4 mm HX double-resonance probe. Prior to the NMR characterization, the Beta zeolite supports were dehydrated under high vacuum ($<10^{-3}$ Pa) by a two-stage temperature ramp (at 1 °C/min to 110 °C, isothermally at 110 °C for 2 h, and at 2 °C/min to 400 °C, isothermally at 400 °C for 12 h), the samples were then transferred into an Ar-filled glove box for NMR sample packing. Single pulse ^{1}H MAS NMR spectra were acquired with a MAS spinning rate of 10 kHz, a 90-degree excitation pulse of 3.0 μs, a recycle delay of 50 s, and each spectrum with a total of 64 scans. The ^{1}H chemical shifts were referenced to adamantane (1.74 ppm).

In situ diffuse reflectance infrared Fourier transform spectroscopy (*in situ* DRIFTS). DRIFTS studies of surface properties of the samples were performed on an FTIR spectrometer (Bruker Vertex 70) with different procedures: 1) to study the surface chemical groups of catalysts, samples were dehydrated in Ar flow at 300 °C for 30 min and before the spectra were recorded at 30 °C; 2) to investigate the changes of hydroxyl groups during *in situ* hydrogen reduction of the Ni catalysts, the samples were treated in Ar-balanced hydrogen flow (5 vol.%) and the spectra were recorded during the temperature ramping from 100 to 400 °C (at 10 °C/min, note that the background is only recorded once at 100 °C); 3) to elucidate the chemical state of Ni catalysts, Ar-balanced 2 vol.% CO was used as probe molecule. The CO-DRIFTS spectra were recorded at 25 °C after purging the catalysts by Ar. Total gas flowrate for all experiments is kept constant at 60 mL/min. Spectra were recorded for 128 scans with resolution of 4 cm^{-1} using the potassium bromide (KBr) as background (256 scans).

X-ray absorption spectrum (XAS). Experiments were conducted on the EasyXAFS300+ laboratory-scale spectrometer (easyXAFS, WA), which uses a Rowland circle optical geometry. Ni K-edge XAFS were acquired using a Si (551) spherically bent crystal analyser (SBCA) and an Ag anode X-ray tube at 40 kV. The X-ray current was varied between 10 to 15 mA (400 – 600 W), depending on the sample to maintain a collection deadtime of < 30%. 13 mm diameter pellets of a known mass of sample were prepared prior to experiment. Pellets were placed onto spectrometer using polymer containing adhesive tape (Scotch® Magic™ Invisible Tape). 4 consecutive scans were performed for all samples, collecting the intensity of the transmitted beam (I_t) and incident beam (I_0) for each sample.

Computational details

DFT simulations were carried out using the FHI-aims package.[2] Single-point energy calculations were performed using the PBEsol[3] functional, with post-processing van der Waals' corrections calculated with the Tkatchenko-Scheffler[4] scheme. For simulations of the periodic unit cells, a $(2 \times 2 \times 2)$ **k**-point Monkhorst-Pack[5] grid was used for sampling of the first-Brillouin zone. The Atomic Simulation Environment (ASE)[6] was used to performed geometry and lattice relaxations. Lattice parameters and atomic positions were relaxed simultaneously through the scheme of Tadmor et al.[7] Strains and forces calculated with FHI-aims using a 'light' basis set,[2] while energetics and other final properties were evaluated using a 'tight' basis set in a post-processing step. The suitability for the above parameters for measuring the energetics of dealuminated zeolites were confirmed in a previous study for Sn incorporation into deAl-Beta.[8]

The initial geometry for the deAl-Beta framework was derived from the work of Navar *et al.*[8] The dealuminated zeolite was modelled by removing the aluminium at T8 and capping the undercoordinated oxygens with hydrogens. Comparisons between the IM and SEA adsorption types were performed with following complexes: $NiCl_2$, $Ni(NO_3)_2$ and $Ni(OH)_2$. Our model was simplified by carrying out simulations in gas phase and electrostatic interactions are the primary driver of interactions between the zeolite and metallic centres. The latter assumption removes the need to include the coordinating H_2O and NH_3 ligands. The IM procedure was modelled using a fully protonated silanol nest. SEA was modelled by deprotonating either one or two of the constituent nested silanols, giving the framework an overall -1 and -2 charge respectively. Washing of the ligands from the metallic centre was modelled by sequentially removing the ligands from simulation cell, where the overall charge of the simulation cell was adjusted as appropriate.

SCF calculations were performed with collinear spin, where Ni was initialised with 2+ charge and a magnetic moment of 2. Deprotonated oxygen sites and ligands were assigned an initial charge of -1. For ligands, this initial charge was distributed evenly among the coordinating oxygens. In some cases, the SCF procedure failed to converge to a single spin state. If so, the system was assumed to be spinless.

The erroneous interaction of the between the net charge of the simulation cell and its periodic images was corrected using the image charge corrections of the Lany-Zunger scheme[9]. This is expressed as **Eq. S1**.

$$E_q^{corr,LZ} = [q + c_{sh}(1-\frac{q}{\varepsilon})]\frac{q^2\alpha_M}{2\varepsilon L}$$

Eq. S1

where q is the overall charge of the simulation cell, c_{sh} is a shape factor accounted for by the dimensions of the simulation cell, ε is the isotropic dielectric constant of the zeolite, α_M is the Madelung constant and $L = \Omega^{-\frac{1}{3}}$ is the linear supercell dimensions, where Ω is the real-space volume of the supercell. ε is taken as 1.81, calculated as an average of the diagonal elements of the dielectric

tensor. The dielectric tensor was calculated via DFPT with the PBE[8] functional for the uncharged deAl-BEA supercell. These calculations were performed using an external workflow to FHI-aims as a Jupyter Notebook. Although the Lany-Zunger correction includes a potential alignment term, this term calculated through the approach of Komsa *et al.*[10] yielded an overall energy change of 0.04 eV for a doubly charged supercell and is therefore neglected.

A further simulation is carried using Quantum Espresso[10-12] to utilise the 3D-RISM[13] solvation model. These simulations were carried out with 33 Ryd kinetic energy cut-off, the PBEsol exchange correlation functional with the Grimme D3 dispersion correction.[14] The core states of the system were represented with the SSP pseudopotentials for PBE.[15] Differences in values between FHI-aims and Quantum Espresso are caused using different dispersion corrections; the many-body dispersion corrections used in the presented FHI-aims simulations is currently unavailable with the ultra-soft pseudopotentials employed in the corresponding Quantum Espresso simulations.

Adsorption energies (ΔE_{ads}) were calculated by taking the total energy difference between the adsorbed complex and zeolite, and the combined energies of the isolated metallic complexes and the de-AlBEA zeolite (**Eq. S2**),

$$\Delta E_{ads} = E(deAlBeta - NiX_2) - (E(X_2) + E(deAl - Beta))$$

Eq. S2

Ion exchange energies (ΔE_{ex}) for the exchange of OH$^-$ with X (where X=NO$_3$, Cl) were calculated by taking the total energy difference between the isolated/adsorbed NiX$_n$ and NiOH$_n$ complexes combined with their respective free anions (**Eq. S3**),

$$\Delta E_{ex} = (E(NiOH_n) + E(nX)) - (E(nX) + E(NiX_2))$$

Eq. S3

where n is the number of ions exchanged.

Catalysis

CO_2 methanation over the developed Ni catalysts was conducted in a fixed-bed reactor with a quartz tube (inner diameter of 4 mm) at atmospheric pressure. In a typical run, 0.1 g granular catalyst (355–500 μm pellet size) was fixed at the centre of reactor tube by glass wool. The feed gas with total flow rate of 50 mL/min (volume ratio of H_2, CO_2 and Ar = 4:1:5) was employed to give a gas hourly space velocity (GHSV) of 30,000 mL/(g·h). The flowrate of outlet stream was measured by a bubbling flowmeter, and its composition was analysed by a two-channel on-line gas chromatography (GC) equipped with an HayeSep DB packed column, a thermal conductivity detector (TCD) and a flame ionisation detector (FID). Ar was used as the carrier gas. And propylene (5000 ppm, 20 sccm) was introduced into GC after the reactor and used as external standard for GC calibration. The peak area ratios of CO_2/Propylene, CH_4/propylene and CO/propylene were used for relevant calculations.

The CO_2 conversion (X_{CO2}) and CH_4 selectivity (S_{CH4}) were defined by **Eq. S4** and **Eq. S5**, respectively.

$$X_{CO2} = \frac{CO_{2,in} - CO_{2,out}}{CO_{2,in}} \times 100\% \qquad \text{Eq. S4}$$

$$S_{CH_4} = \frac{CH_{4,out}}{CO_{2,in} - CO_{2,out}} \times 100\% \qquad \text{Eq. S5}$$

where the $CO_{2,in}$ and $CO_{2,out}$ is the molar flow rate (mol/s) of CO_2 in the feed and outlet of the reactor.

The $CH_{4,out}$ is the molar flow rate (mol/s) of CH_4 in the outlet of reactor.

The specific reaction rate was calculated using **Eq. S6**.

$$r_{CO_2} = \frac{CO_{2,in} \cdot X_{CO_2}}{W_{Ni}} \qquad \text{Eq. S6}$$

where r_{CO_2} is the conversion rate of CO_2 (mol /(s·g_{Ni})) and W_{Ni} is the mass of Ni in the catalyst (g).

Calculation of dispersion according to TEM analysis

In determination of metal dispersion by **chemisorption (e.g., CO/H$_2$)**, the metal dispersion (D) is defined as:

$$SA_{metal} = [\frac{V_{ads}}{V_m}] \cdot SF \cdot N_A \cdot A_{\varnothing,metal}$$

Eq. S7

$$D = [\frac{V_{ads} \cdot SF}{V_m}] \cdot M_w$$

Eq. S8

where SA_{metal} is the metallic surface area, V_{ads} is the volume of adsorbed probe molecules, V_m is the molar volume of gas, SF is the stoichiometric factor of the number of adsorbed probe molecules (V_{ads}) per metallic surface atom, N_A is the Avogadro's constant, $A_{\varnothing,metal}$ is the across-sectional area of metal, D is the metal dispersion and M_w is the atomic mass.

Combining **Eq. S7** and **Eq. S8, Eq. S9** can be obtained as:

$$SA_{metal} = [\frac{D}{M_w}] \cdot N_A \cdot A_{\varnothing,metal}$$

Eq. S9

Eq. S10 can be employed to estimate SA_{metal} by **physical method (i.e., TEM)**.

$$SA_{metal} = \frac{A_{NP}}{V_{NP} \cdot \rho}$$

Eq. S10

where A_{NP} is the surface area of metal NP, V_{NP} is the volume of metal NPs, and ρ is the metal density.

Assuming that the metal NPs sit on the carrier surface as hemispheres with medium metal-support interaction (standard assumption in particle size determination[16]), Eq. S10 can be converted to **Eq. 11**.

$$SA_{metal} = \frac{6}{\rho \cdot d}$$

Eq. S11

where d is the mean diameter of metal NPs.

By equating Eq. S9 and Eq. S10, metal dispersion (D) can be estimated by **Eq. S12**.

$$D = 6 \cdot \left(\frac{v_m}{a_m}\right) \cdot \frac{1}{d} \qquad \text{Eq. S12}$$

where the a_m is surface area occupied by a metal atom, and v_m is volume occupied by a metal atom.

The a_m and v_m can be calculated by **Eq. S13** and **Eq. S14**, respectively.

$$a_m = \frac{1}{n_s} \qquad \text{Eq. S13}$$

$$v_m = \frac{M_w \cdot n}{\rho \cdot N_A} \qquad \text{Eq. S14}$$

where n_s is mean number of atoms per unit area, which can be calculated from simple crystal systems. For the case of Ni, it is face center cubic (FCC) structure with lattice parameter of a = b = c = 0.352 nm, and α = β = γ = 90°.

For plane (111), the metal surface area is $\dfrac{a^2\sqrt{3}}{2}$ and number of atoms is 2.

For plane (100), the metal surface area is a^2 and number of atoms is 2.

For plane (110), the metal surface area is $\dfrac{a^2}{\sqrt{2}}$ and number of atoms is 2.

The calculation result of n_s is shown as below:

Plane	Area (m²)	Atom per cell (atoms)	Atom per area (atoms/m²)
(111)	1.07×10−19	2	1.86×1019
(100)	1.24×10−19	2	1.61×1019
(110)	1.75×10−19	2	1.14×1019
Mean number of atoms per unit area, n_s			1.54×1019

$$v_m = \frac{M_w \cdot n}{\rho \cdot N_A} = \frac{58 \times 1 \times 10^{-6}}{8.908 \times 6.02 \times 10^{23}} = 1.08 \times 10^{-29} (m^3)$$

Then, Eq. S12 can be simplified to **Eq. S15** for the estimation of Ni dispersion of the catalysts under investigation.

$$D = 6 \cdot \left(\frac{1.08 \times 1.54 \times 10^{-29}}{10^{-19}}\right) \cdot \frac{1}{d} = \frac{99.8}{d} \qquad \text{Eq. S15}$$

Accordingly, the Ni dispersion of Ni-Cl@deAl-Beta-SEA (3.5 nm) and Ni-Cl/deAl-beta-IM (23.3 nm) was calculated as about 29% and 4%, respectively.
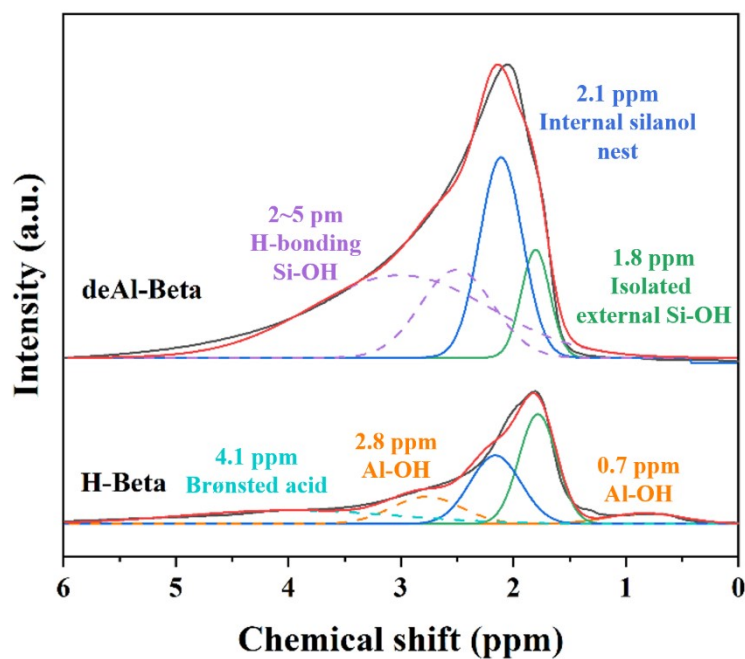
Supporting Figures and Discussions

Figure S1. ^{1}H NMR spectra of H-Beta and deAl-Beta.

^{1}H NMR analysis of H-Beta and deAl-Beta shows that dealumination of H-Beta resulted in elimination of Brønsted acid sites (at ~4.0 ppm) and Al-OH (at ~0.7 and ~2.8 ppm), while formation of silanol nest (at ~2.0 ppm) and hydrogen-bonding Si-OH (broad peak at 2~5 ppm) was identified.

Figure S2. NiCl$_2$ and Ni(NH$_3$)$_6$Cl$_2$ solution.

The color of NiCl$_2$ solution changed from light green to light blue (Ni(NH$_3$)$_6$Cl$_2$) upon the addition of ammonium hydroxide solution.
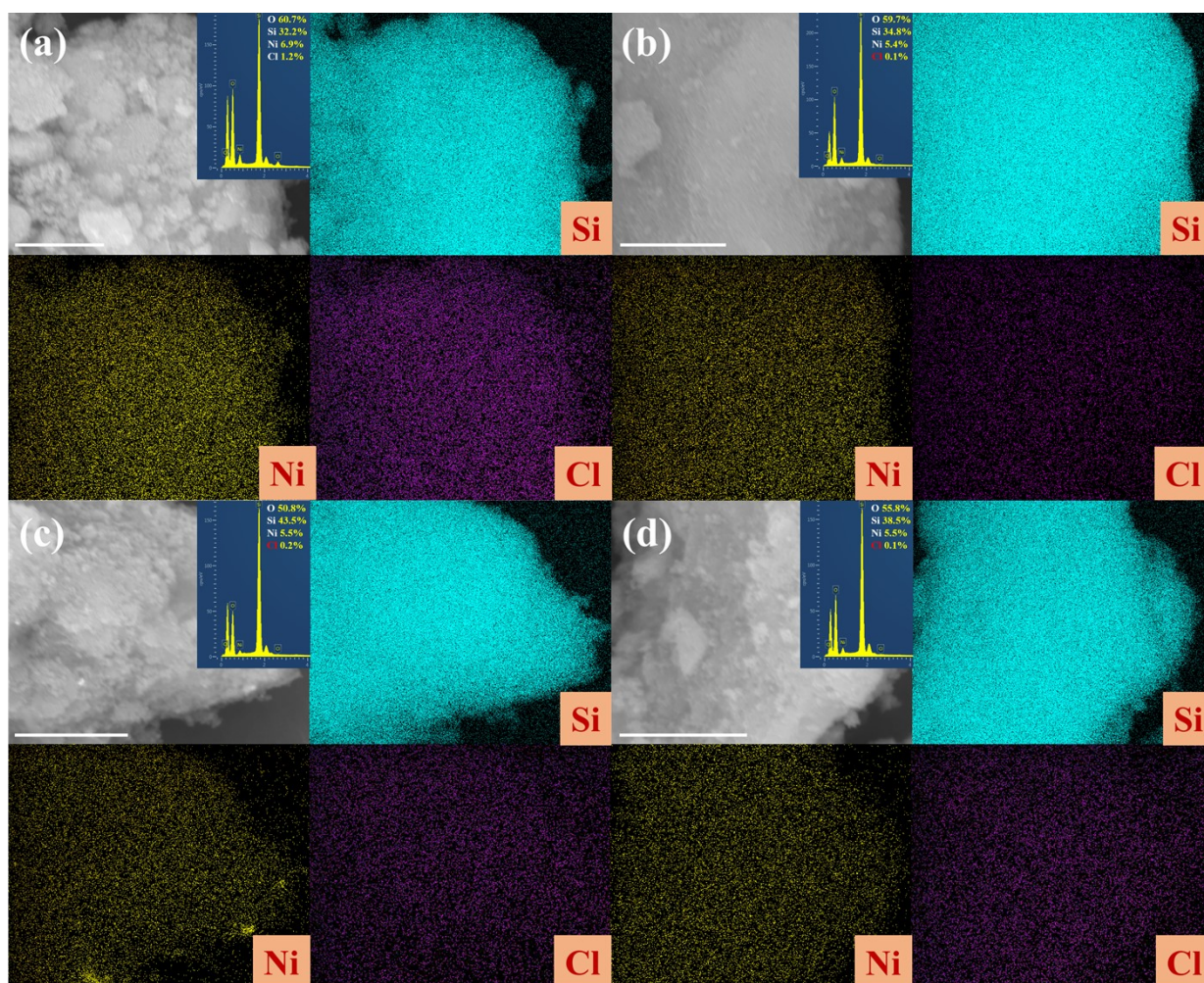
Figure S3. SEM-EDX mapping analysis of the as-prepared and reduced (a, c) Ni-Cl/deAl-Beta-IM and (b, d) Ni-Cl@deAl-Beta-SEA. Scale bars in all images is 5 μm.

The as-prepared Ni-Cl/deAl-Beta-IM possessed relatively high Cl^- content (~1.2 wt.%), whilst Ni-Cl@deAl-Beta-SEA only showed trace amount of Cl^- (~0.1 wt.%). After reduction, distinct Ni agglomeration could be observed in Ni-Cl/deAl-Beta-IM, while the Ni species in Ni-Cl/deAl-Beta-IM remained highly dispersed.
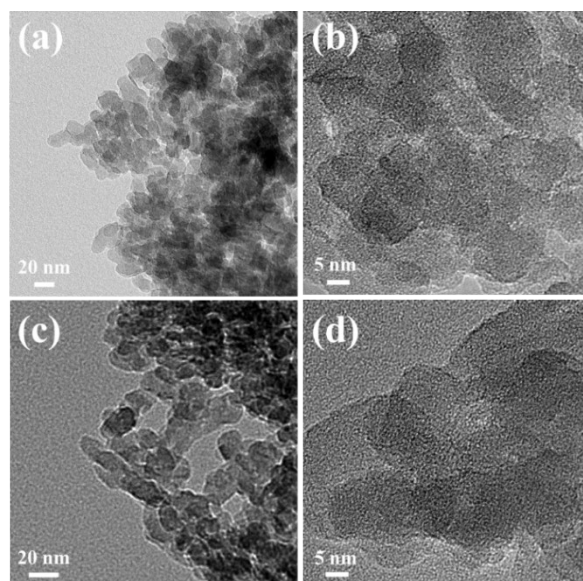

Figure S4. TEM images of (a, b) H-Beta and (c, d) deAl-Beta.

The deAl-Beta shows similar morphology to H-Beta, which consists of nanocrystals with grain size of about 20 nm.
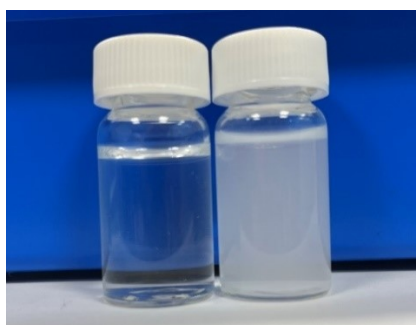

Figure S5. The test for the presence of chlorides in the liquid sample from the SEA synthesis of Ni-Cl@deAl-Beta-SEA (after centrifugation). Bottle on the left = the solution before titration; bottle on the right = the solution titrated solution using 0.1 mol/L silver nitrate solution.

The Ag test using silver nitrate solution confirmed the presence of Cl⁻ anion in the solution after the SEA synthesis.
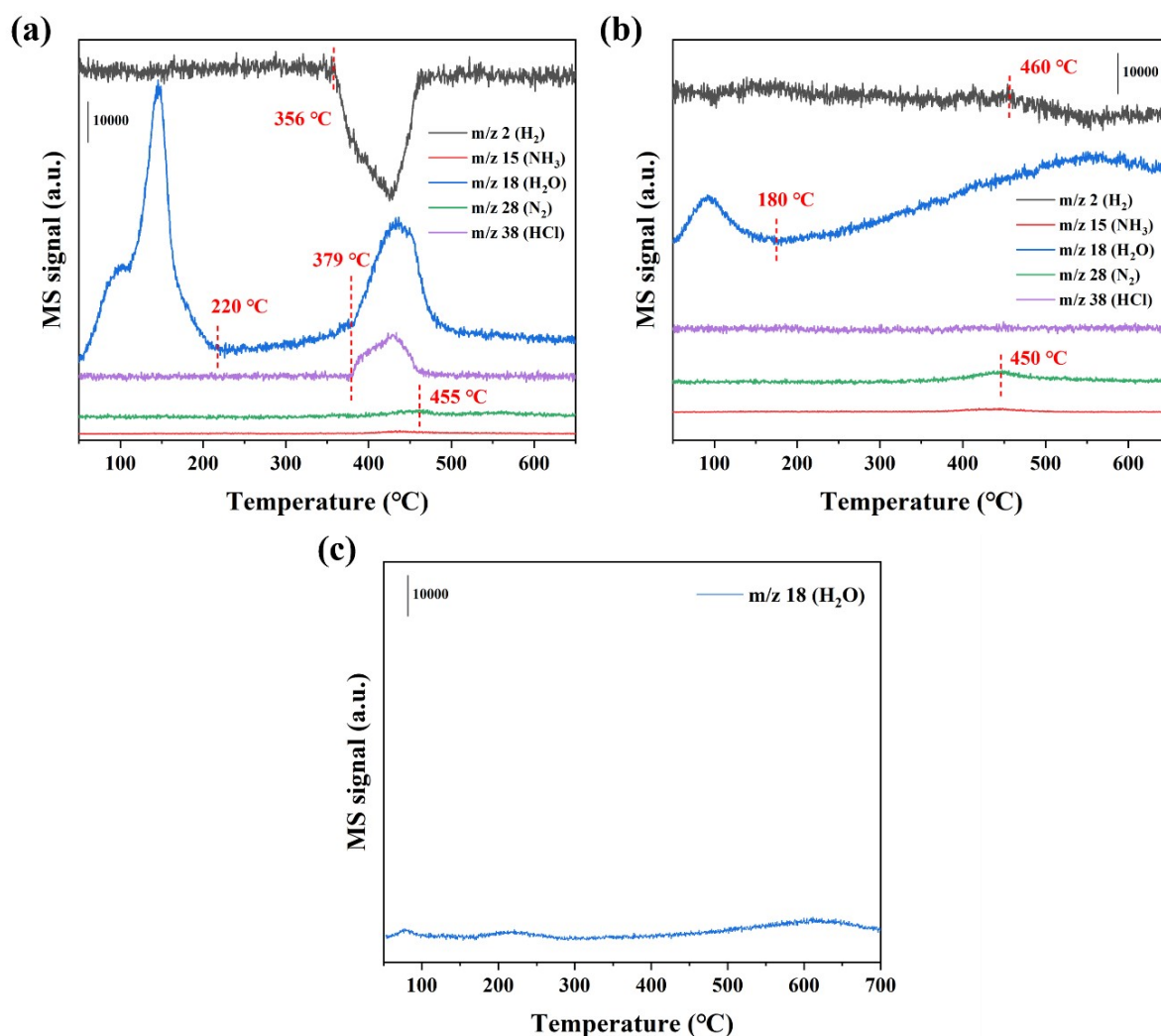

Figure S6. Species evolution during the reduction of Ni catalysts studied by in situ H_2-TPR-MS of (a) Ni-Cl/deAl-Beta-IM, (b) Ni-Cl@deAl-Beta-SEA and (c) deAl-Beta.
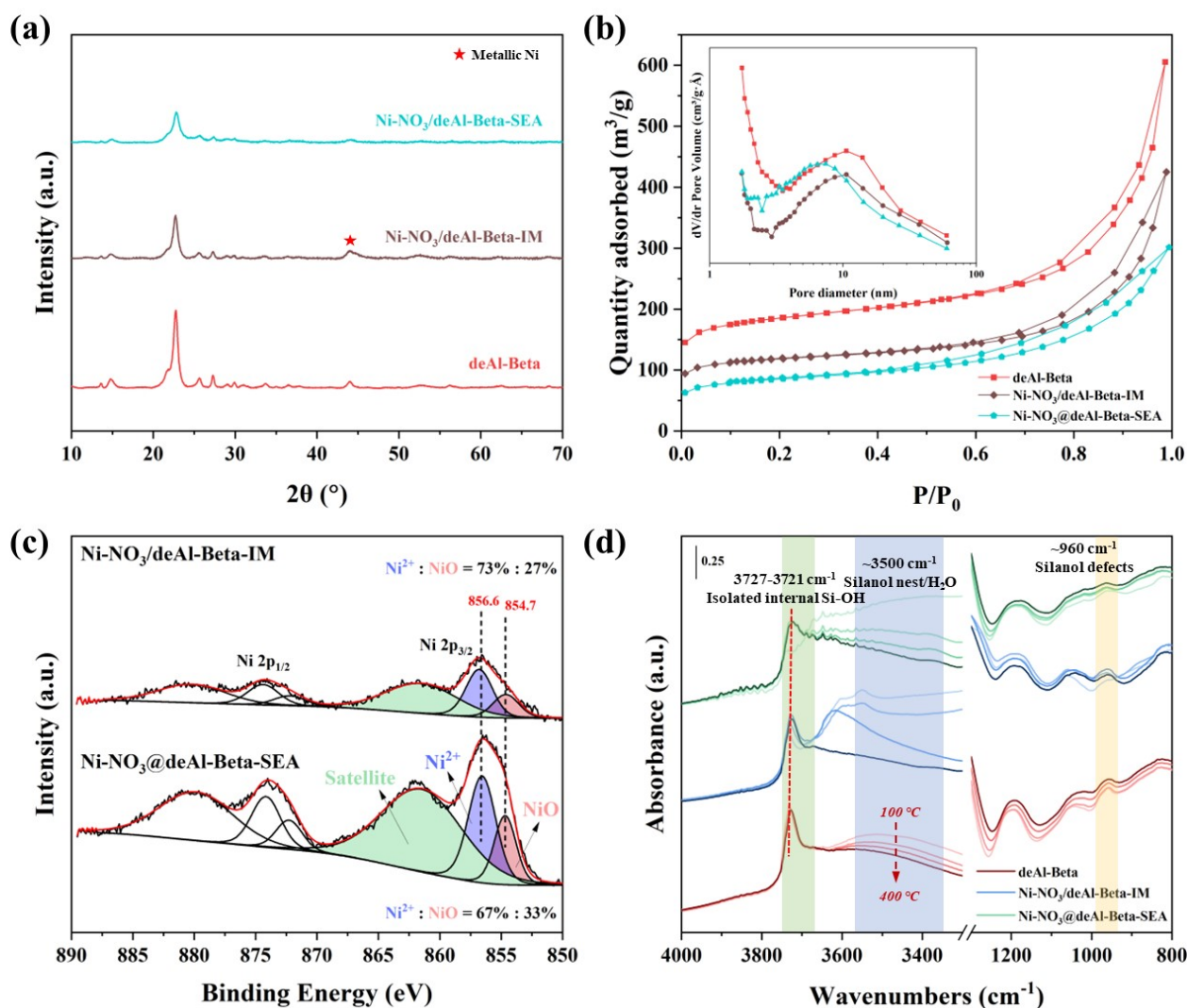
Figure S7. Characterizations of Ni catalysts prepared by SEA and IM using $Ni(NO_3)_2$ as precursor: (a) XRD, (b) N_2 physisorption, (c) XPS and (d) *in situ* DRIFTS of catalyst reduction.

Similar features to catalysts prepared by $NiCl_2$ were found, including: 1) noticeable XRD diffraction peak at ca. 44.8° assigning to relatively large Ni crystalline in Ni-NO$_3$/deAl-Beta-IM; 2) more reduction of porosity in Ni-NO$_3$@deAl-Beta-SEA than Ni-NO$_3$/deAl-Beta-IM; 3) stronger peak intensity of XPS Ni 2p spectra and more NiO species in Ni-NO$_3$@deAl-Beta-SEA and 4) more significant red-shift and broadening of isolated Si-OH and reduction of silanol nest at ~960 cm^{-1} in Ni-NO$_3$@deAl-Beta-SEA during catalyst reduction.
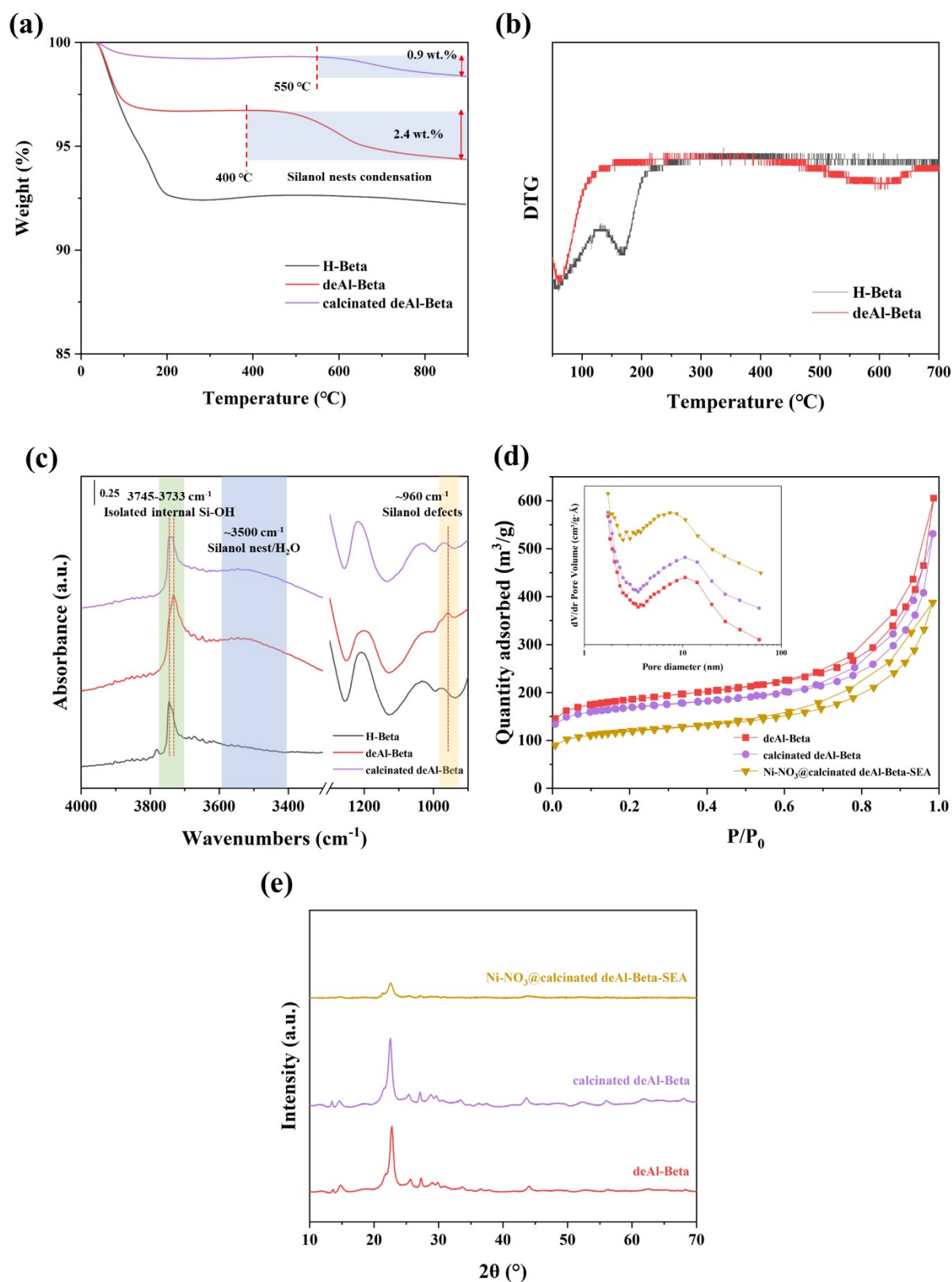
Figure S8. Characterizations of calcinated deAl-Beta and the supported Ni catalyst. (a) TGA (in O_2), (b) DTG, (c) DRIFTS spectra (recorded at 30 ℃ after pretreatment at 300 ℃), (d) N_2 physisorption and (e) XRD.

TG analysis shows that the H-Beta only exhibits a single event relating to the water removal at temperature <200 ℃, while deAl-Beta exhibits distinct weight loss (~2.4 wt.%) at temperature between 400 to 900 ℃, which is ascribed to the condensation of silanol defects. Calcinated Beta shows weight loss of ~0.9 wt.% at temperature between 550 to 900 ℃,

indicating that the silanol defects were decreased after calcination at 550 ℃. DTG shows significant weight loss in deAl-Beta occurs at ca. 600 ℃ and ends at ca. 700 ℃. DRIFTS of calcinated deAl-Beta shows distinct intensity decrease and narrowing of the band at 3733 to 3745 cm⁻¹ (isolated internal Si-OH with weak hydrogen-bonding), slight decrease of band at 3500 cm⁻¹ and blue-shift of band at 960 cm⁻¹ (silanol defect). In combination, the calcinated deAl-Beta displays less hydroxyl groups than the pristine deAl-Beta (i.e., partly healed silanol defects).
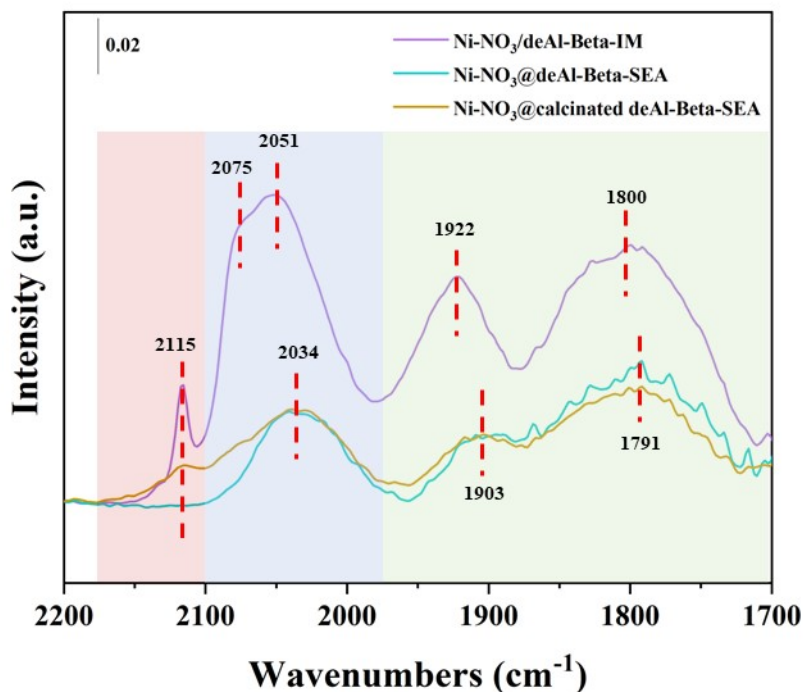
Figure S9. *In situ* CO-DRIFTS of Ni catalysts at 30 ℃ prepared by different methods (IM or SEA) and supported on deAl-Beta with different silanol nest abundancy (i.e., pristine and calcinated deAl-Beta).
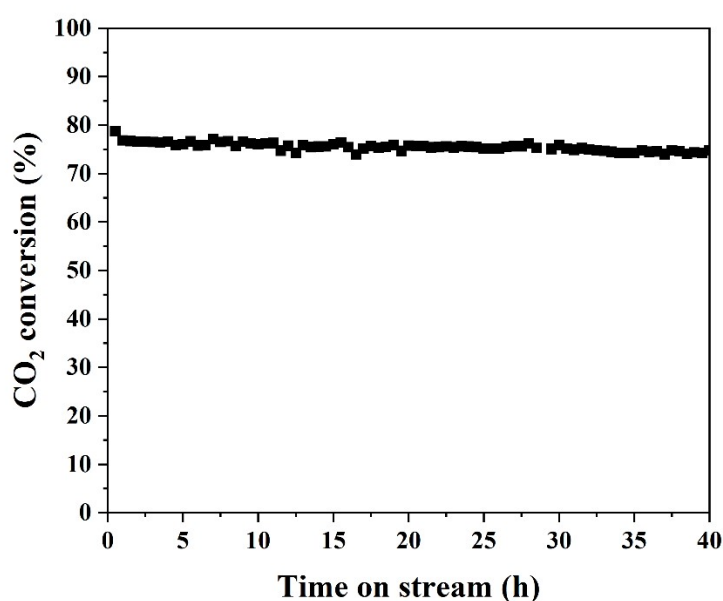
Figure S10. Longevity test of Ni-NO$_3$@deAl-Beta-SEA. Reaction conditions: H$_2$, CO$_2$ and Ar flow rates of 20, 5 and 25 mL min⁻¹, 400 ℃, ~0.1 g catalyst, and GHSV of 30,000 mL g⁻¹ h⁻¹.

Figure S11. TEM of used Ni-NO$_3$@deAl-Beta-SEA after 40-h longevity test. The particle size distribution of the studied catalysts was based on statistics of counting *ca.* 100 particles from relevant HRTEM images (using ImageJ).

Supporting Tables and Discussion

Table S1. Porous properties and metal loading of deAl-Beta and Ni/Pt catalysts.

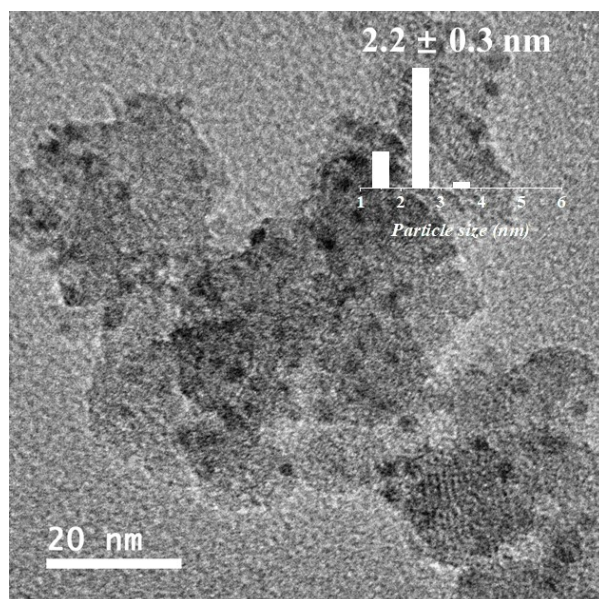| Sample	Si/Al	Ni loading (wt.%)	Specific surface area (m^2/g)			Specific pore volumes (cm^3/g)		
			S$_{BET}$	S$_{micro}$	S$_{meso}$	V$_{total}$	V$_{micro}$	V$_{meso}$
deAl-Beta	> 1000[a]	n.a.	582	361	221	0.76	0.19	0.57
NH$_4$OH-treated deAl-Beta	n.a.	n.a.	387	202	185	0.71	0.10	0.61
Calcinated deAl-Beta[b]	n.a.	n.a.	525	344	181	0.58	0.18	0.4
Ni-Cl@deAl-Beta-SEA	n.a.	7.92[c]	446	184	261	0.70	0.09	0.61
Ni-Cl/deAl-Beta-IM	n.a.	11.71	545	339	206	0.70	0.17	0.53
Ni-NO$_3$@deAl-Beta-SEA	n.a.	7.12	274	135	139	0.38	0.07	0.31
Ni-NO$_3$/deAl-Beta-IM	n.a.	10.16	369	241	128	0.47	0.13	0.34
Ni-NO$_3$@calcinated deAl-Beta-SEA	n.a.	7.67	376	210	166	0.48	0.11	0.37

[a] Measured by ICP.

[b] The deAl-Beta was treated in the same NH$_4$OH solution but without the addition of Ni precursor to study destructive effect of alkaline treatment on zeolite structure. The specific surface areas and pore volumes of the NH$_4$OH-treated deAl-Beta was reduced comparing to that of deAl-Beta, which was due to dissolution of zeolite framework by NH$_4$OH solution starting from the defective silanol sites.[17] Comparatively, the Ni-Cl@deAl-Beta-SEA shows the rather preserved porosity compared to that of the NH$_4$OH treated deAl-Beta, suggesting that in the SEA synthesis the Ni ammine cations (Ni(NH$_3$)$_6$$^{2+}$) could interact with relevant silanol sites on deAl-Beta, acting as the pore moderator to inhibit the dissolution of zeolitic framework in alkaline solution.

[c] The Ni catalysts prepared by SEA generally show less actual Ni content (7~8 wt.%) than that of IM (~10 wt.%), which is probably due to the saturation adsorption of metal ions in deAl-Beta.

Table S2. Comparison of the synthesis methods for preparing the supported Ni NPs on zeolitic carriers and relevant properties of supported Ni NPs.

Samples	Synthesis method	Ni loading (%)	Thermal treatment	Size (nm)	Refs.
Ni/silicalite-2	Encapsulation using ligand-protected metal precursor	0.3	550 °C (air)	2.6 ± 0.9	[18]
Ni/deAl-beta-IM	Impregnation	10	400 °C (air)	7.3	[19]
Ni/NH$_4$-Beta	Ion exchange-deposition-precipitation	6.2	550 °C (air)	3.5	[20]
Ni/HZSM-5	Encapsulation (using Ni/SiO$_2$ as unique silicone source)	10	550 °C (air)	7.6	[21]
Ni-La$_2$O$_3$/Na-Beta	Impregnation with promoter	10	550 °C (air)	7.1	[22]
Ni/USY	Impregnation	15	500 °C (air)	18 ± 4	[23]

Ni/Beta	Deposition-precipitation using hierarchical zeolite	40	500 °C (air)	5.6 ± 1.3	24
Ni-Cl@deAl-Beta-SEA	Strong electrostatic adsorption	10	500 °C (H$_2$)	3.5 ± 0.4	This work
Ni-NO$_3$@deAl-Beta-SEA	Strong electrostatic adsorption	10	500 °C (H$_2$)	1.9 ± 0.2	This work

Table S3. Comparison of CO$_2$ methanation performance over different supported Ni catalysts at 400°C.

Sample	Preparation conditions	Ni size (nm)	GHSV (mL g^{-1} h^{-1})	X$_{CO2}$ (%)	S$_{CH4}$ (%)	r_{CO2} (10^{-4}×mol^{-1} s^{-1} g$_{Ni}$$^{-1}$)	Refs.
Ni/SiO$_2$	Impregnation (nickel acetate); calcination (500 °C, 5 h); reduction (500 °C, 3 h)	33	12,000	60	88	0.89	25
Ni/ZrO$_2$-CNT	Impregnation (nickel nitrate); calcination (350 °C, 5 h); reduction (500 °C, 1 h)	n.a.	75,000	55	97	0.27	26
Ni/ZrO$_2$	Impregnation (nickel nitrate); decomposition in plasma (1 h); reduction (500 °C, 1 h)	9	48,000	77	99	10.7	27
Ni/Al$_2$O$_3$-ZrO$_2$	One-pot sol gel method (nickel nitrate); calcination (550 °C, 6 h); reduction (50 °C, 10 h)	n.a.	6,000	72	99	1.0	28
Ni/13 A zeolite	Impregnation (nickel citrate); calcination (450 °C, 3h); reduction (500 °C, 4 h)	n.a.	13,000	73	96	1.2	29
Ni/deAl-Beta	Impregnation (nickel nitrate); calcination (400 °C, 3 h); reduction (600 °C, 2 h)	7.3	30,000	82	99	4.7	19
Ni/Na-Beta	Impregnation (nickel nitrate); calcination (550 °C, 6 h); reduction (500 °C, 1 h)	17	4,800	60	93	0.58	22
Ni/hollow H-ZSM-5	Impregnation (nickel nitrate); calcination (550 °C, 6 h); reduction (500 °C, 3 h)	9~21	12,000	78.5	99	1.56	30
La$_2$O$_3$/Ni/ZSM-5 (plate-like)	Impregnation (nickel nitrate); calcination (550 °C, 6 h); reduction (500 °C, 3 h)	65	12,000	63	98	1.25	31

References

[1]   C. Hammond, S. Conrad, I. Hermans, *Angew. Chem. Int. Ed. Engl.,* 2012, **51**, 11736-11739.

[2]   V. Blum, R. Gehrke, F. Hanke, P. Havu, V. Havu, X. Ren, K. Reuter, M. Scheffler, *Computer Physics Communications,* 2009, **180**, 2175-2196.

[3]   J. P. Perdew, A. Ruzsinszky, G. I. Csonka, O. A. Vydrov, G. E. Scuseria, L. A. Constantin, X. Zhou, K. Burke, *Physical Review Letters,* 2008, **100**, 136406.

[4]   A. Tkatchenko, R. A. DiStasio, R. Car, M. Scheffler, *Physical Review Letters,* 2012, **108**, 236402.

[5]   H. J. Monkhorst, J. D. Pack, *Physical Review B,* 1976, **13**, 5188-5192.

[6]   A. H. Larsen, J. J. Mortensen, J. Blomqvist, I. E. Castelli, R. Christensen, M. Dułak, J. Friis, M. N. Groves, B. Hammer, C. Hargus, E. D. Hermes, P. C. Jennings, P. B. Jensen, J. Kermode, J. R. Kitchin, E. L. Kolsbjerg, J. Kubal, K. Kaasbjerg, S. Lysgaard, J. B. Maronsson, T. Maxson, T. Olsen, L. Pastewka, A. Peterson, C. Rostgaard, J. Schiøtz, O. Schütt, M. Strange, K. S. Thygesen, T. Vegge, L. Vilhelmsen, M. Walter, Z. Zeng, K. W. Jacobsen, *Journal of Physics: Condensed Matter,* 2017, **29**, 273002.

[7]   E. B. Tadmor, G. S. Smith, N. Bernstein, E. Kaxiras, *Physical Review B,* 1999, **59**, 235-245.

[8]   R. Navar, G. Tarantino, O. T. Beynon, D. Padovan, L. Botti, E. K. Gibson, P. P. Wells, A. Owens, S. A. Kondrat, A. J. Logsdail, C. Hammond, *Journal of Materials Chemistry A,* 2022, **10**, 22025-22041.

[9]   S. Lany, A. Zunger, *Physical Review B,* 2008, **78**, 235104.

[10]   H.-P. Komsa, T. T. Rantala, A. Pasquarello, *Physical Review B,* 2012, **86**, 045112.

[11]   P. Giannozzi, S. Baroni, N. Bonini, M. Calandra, R. Car, C. Cavazzoni, D. Ceresoli, G. L. Chiarotti, M. Cococcioni, I. Dabo, A. Dal Corso, S. de Gironcoli, S. Fabris, G. Fratesi, R. Gebauer, U. Gerstmann, C. Gougoussis, A. Kokalj, M. Lazzeri, L. Martin-Samos, N. Marzari, F. Mauri, R. Mazzarello, S. Paolini, A. Pasquarello, L. Paulatto, C. Sbraccia, S. Scandolo, G. Sclauzero, A. P. Seitsonen, A. Smogunov, P. Umari, R. M. Wentzcovitch, *Journal of Physics. Condensed Matter: An Institute of Physics Journal,* 2009, **21**, 395502.

[12]   P. Giannozzi, O. Andreussi, T. Brumme, O. Bunau, M. Buongiorno Nardelli, M. Calandra, R. Car, C. Cavazzoni, D. Ceresoli, M. Cococcioni, N. Colonna, I. Carnimeo, A. Dal Corso, S. de Gironcoli, P. Delugas, R. A. DiStasio, A. Ferretti, A. Floris, G. Fratesi, G. Fugallo, R. Gebauer, U. Gerstmann, F. Giustino, T. Gorni, J. Jia, M. Kawamura, H.-Y. Ko, A. Kokalj, E. Küçükbenli, M. Lazzeri, M. Marsili, N. Marzari, F. Mauri, N. L. Nguyen, H.-V. Nguyen, A. Otero-de-la-Roza, L. Paulatto, S. Poncé, D. Rocca, R. Sabatini, B. Santra, M. Schlipf, A. P. Seitsonen, A. Smogunov, I. Timrov, T. Thonhauser, P. Umari, N. Vast, X. Wu, S. Baroni, *Journal of Physics. Condensed Matter: An Institute of Physics Journal,* 2017, **29**, 465901.

[13]   H. Sato, A. Kovalenko, F. Hirata, *The Journal of Chemical Physics,* 2000, **112**, 9463-9468.

[14]   S. Grimme, J. Antony, S. Ehrlich, H. Krieg, *The Journal of Chemical Physics,* 2010, **132**, 154104.

[15]   G. Prandini, A. Marrazzo, I. E. Castelli, N. Mounet, N. Marzari, *npj Computational Materials,* 2018, **4**, 1-13.

[16]   L. Torrente-Murciano, *J. Nanopart. Res.,* 2016, **18**, 87.

[17]   J. Van Aelst, M. Haouas, E. Gobechiya, K. Houthoofd, A. Philippaerts, S. P. Sree, C. E. A. Kirschhock, P. Jacobs, J. A. Martens, B. F. Sels, F. Taulelle, *J. Phys. Chem. C,* 2014, **118**, 22573-22582.

[18]   J. Wang, Y. Fu, W. Kong, F. Jin, J. Bai, J. Zhang, Y. Sun, *Appl. Catal. B,* 2021, **282**, 119546.

[19]   W. Gac, W. Zawadzki, G. Słowik, M. Kuśmierz, S. Dzwigaj, *Appl. Surf. Sci.,* 2021, **564**, 150421.

[20]   P. Yan, J. Mensah, A. Adesina, E. Kennedy, M. Stockenhuber, *Appl. Catal. B,* 2020, **267**, 118690.

[21]   Y. Chen, B. Qiu, Y. Liu, Y. Zhang, *Appl. Catal. B,* 2020, **269**, 118801.

[22]   A. Quindimil, U. De-La-Torre, B. Pereda-Ayo, J. A. González-Marcos, J. R. González-Velasco, *Appl. Catal. B,* 2018, **238**, 393-403.

[23]   M. C. Bacariza, I. Graça, J. M. Lopes, C. Henriques, *Microporous Mesoporous Mater.,* 2018, **267**, 9-19.

[24]   B. Ma, J. Hu, Y. Wang, C. Zhao, *Green Chem.,* 2015, **17**, 4610-4617.

[25]   X. Wen, L. Xu, M. Chen, Y. Shi, C. Lv, Y. Cui, X. Wu, G. Cheng, C.-e. Wu, Z. Miao, F. Wang, X. Hu, *Appl. Catal. B,* 2021, **297**, 120486.

[26]   M. Romero-Sáez, A. B. Dongil, N. Benito, R. Espinoza-González, N. Escalona, F. Gracia, *Appl. Catal. B,* 2018, **237**, 817-825.

[27]   X. Jia, X. Zhang, N. Rui, X. Hu, C.-j. Liu, *Appl. Catal. B,* 2019, **244**, 159-169.

[28] J. Lin, C. Ma, Q. Wang, Y. Xu, G. Ma, J. Wang, H. Wang, C. Dong, C. Zhang, M. Ding, *Appl. Catal. B,* 2019, **243**, 262-272.

[29] L. Wei, W. Haije, N. Kumar, J. Peltonen, M. Peurla, H. Grenman, W. de Jong, *Catal. Today,* 2021, **362**, 35-46.

[30] Y. Cui, B. Chen, L. Xu, M. Chen, C.-e. Wu, J. Qiu, G. Cheng, N. Wang, J. Xu, X. Hu, *Fuel,* 2023, **334**, 126783.

[31] Y. Cui, J. Qiu, B. Chen, L. Xu, M. Chen, C.-e. Wu, G. Cheng, B. Yang, N. Wang, X. Hu, *Fuel,* 2022, **324**, 124679.